Reconstruction of Temperature, Accumulation Rate, and Layer Thinning from an Ice Core at South Pole Using a Statistical Inverse Method

Emma C. Kahle[1], Eric J. Steig[1], Tyler R. Jones[2], T.J. Fudge[1], Michelle R. Koutnik[1], Valerie Morris[2], Bruce H. Vaughn[2], Andrew J. Schauer[1], C. Max Stevens[1], Howard Conway[1], Edwin D. Waddington[1], Christo Buizert[3], Jenna Epifanio[3], James W. C. White[2]

[1]Department of Earth and Space Sciences, University of Washington, Seattle WA 98195, USA

[2]Institute of Arctic and Alpine Research, University of Colorado, Boulder CO 80309, USA

[3]College of Earth Ocean and Atmospheric Sciences, Oregon State University, Corvallis OR 97331, USA

Contents of this file

1. Text S1 to S5
2. Figures S1 to S11

Corresponding author: E. J. Steig, Department of Earth and Space Sciences, University of Washington, Seattle WA 98195, USA. (steig@uw.edu)

Introduction This supporting information document provides further details on the methods and analysis described in the main text. We include information about:

S1. Diffusion-length data and modeling

S2. Inverse methods

S3. Sensitivity tests

S4. Ice-flow modeling

S5. δ^{15}N-based thinning function

Text S1. Diffusion-length data and modeling

S1.1 Corrections to diffusion-length data

We make two corrections to the estimates of diffusion length calculated from the spectra of the water-isotope data.

First, we correct for the effect on the water-isotope data from the continuous-flow-analysis (CFA) measurement system. As melted ice samples are transported through the tubing and reservoirs of the CFA system, some smoothing of the high-frequencies of the natural water-isotope variations occurs. This smoothing is minimized by design of the components of the CFA-system, but still impacts the measured signal. The extent of this system smoothing can be quantified by measuring the system response to a step change in isotopic value using laboratory-produced ice (Jones et al., 2017b). The system diffusion length for the CFA system used in this analysis is 0.07 cm for δ^{17}O and δ^{18}O, and 0.08 cm for δD (Jones et al., 2017b).

Second, we correct for the additional diffusion that occurred in the solid ice below the bottom of the firn, following Gkinis et al. (2014). To calculate the solid-ice diffusion length, we assume the modern borehole temperature profile $T(z)$ remains constant through time to find the diffusivity profile $D_{ice}(z)$, following Gkinis et al. (2014):

$$D_{ice}(z) = 9.2 \times 10^{-4} \times \exp\left(\frac{-7186}{T(z)}\right), \tag{1}$$

with $T(z)$ given in K and $D_{ice}(z)$ given in m^2 s^{-1}. For $T(z)$ at SPC14, we use borehole temperature measurements from the nearby neutrino observatory (Price et al., 2002).

The solid-ice diffusion length is also affected by vertical strain in the ice sheet. We assume a simple thinning function from a 1-D ice-flow model (Dansgaard and Johnsen, 1969) with a kink-height $h_0 = 0.2$ for this calculation. We describe the total thinning experienced by a layer $S(t)$ in a given time interval $t = 0$ to $t = t'$ as:

$$S(t') = \exp\left(\int_0^{t'} \dot{\epsilon}_z(t)dt\right), \tag{2}$$

where $\dot{\epsilon}_z(t)$ is the vertical strain rate calculated from the thinning function.

The solid-ice diffusion length, σ_{ice}, is then calculated as (Gkinis et al., 2014):

$$\sigma_{ice}^2(t') = S(t')^2 \int_0^{-t} 2D_{ice}(t)S(t)^{-2}dt. \tag{3}$$

To produce the corrected diffusion-length data set used in this analysis, we subtract in quadrature both the system diffusion length, σ_{CFA}, and the solid-ice diffusion length, σ_{solid}, from the total measured diffusion length, σ_{meas}:

$$\sigma^2 = \sigma_{meas}^2 - \sigma_{CFA}^2 - \sigma_{solid}^2. \tag{4}$$

The diffusion length σ represents the diffusion that occurred within the firn column and that has experienced the effects of vertical strain in the ice sheet ($i.e.$ $\sigma = S(z)\sigma_{firn}$).

Figure S1 shows the effect of these corrections on the estimated diffusion length.

S1.2 Modeling firn diffusion length

Within the forward model of the inverse problem, we model diffusion length in the firn column. We use the following values in calculating the diffusivity coefficients, D_x, for each water-isotope ratio:

$$
\begin{aligned}
D^{air}_{\delta^{18}O} &= \frac{D^{air}}{1.0285} && \text{(Johnsen et al., 2000)}\\
D^{air}_{\delta^{17}O} &= \frac{D^{air}}{1.01466} && \text{(Luz and Barkan, 2010)}\\
D^{air}_{\delta D} &= \frac{D^{air}}{1.0251} && \text{(Johnsen et al., 2000)}
\end{aligned}
$$

where:

$$
D^{air} = 0.211 \times 10^{-4} \times \left(\frac{T}{273.15}\right)^{1.94} \times \frac{P_0}{P} \quad \text{(Johnsen et al., 2000)}
$$

is the diffusivity of water vapor in air. T is temperature given in Kelvin and P is the atmospheric pressure compared to a reference pressure of $P_0 = 1$ atm.

We use the following values in calculating the fractionation factors, α_x, for each water-isotope ratio, for the equilibrium of water vapor over ice:

$$
\begin{aligned}
\alpha_{18} &= \exp(\frac{11.839}{T} - 28.224 \times 10^{-3}) && \text{(Majoube, 1970)}\\
\alpha_{17} &= \exp(0.529 \times \log(\alpha_{18})) && \text{(Barkan and Luz, 2007)}\\
\alpha_{D} &= \exp(-0.0559 + \frac{13525}{T^2}) && \text{(Lamb et al., 2017)}
\end{aligned}
$$

The tortuosity parameter τ used in Equation 5 in the main text is given by (Schwander et al., 1988; Johnsen et al., 2000):

$$\frac{1}{\tau} = \begin{cases} 1 - b \times \left(\frac{\rho}{\rho_{ice}}\right)^2 & \text{, for } \rho \leq \frac{\rho_{ice}}{\sqrt{b}} \\ 0 & \text{, for } \rho > \frac{\rho_{ice}}{\sqrt{b}} \end{cases}$$

using a tortuosity parameter $b = 1.3$.

The solution to Equation 4 in the main text for the isotope profile at a given depth z and time t is given by:

$$\delta(z,t) = S(t)\frac{1}{\sigma\sqrt{2\pi}}\int_{-\infty}^{\infty} \delta(z,0)\exp\left(\frac{-(z-u)^2}{2\sigma^2}\right) du, \tag{5}$$

as described in (Gkinis et al., 2014) and fully derived in Kahle et al. (2020), where σ is the diffusion length and the factor $S(t)$ is the total thinning a layer has experienced due to ice flow, as described in Equation 2 of this supplement.

Text S2. Inverse methods

The statistical inverse method used in this work relates the three variables that span the model space with the three data variables that span the data space. We define the model space as a vector space with a dimension for each of the unknown input parameters; a particular point in the model space represents a specific set of input parameters m. The data space is defined similarly, where each data parameter in d represents a dimension, and our observations d_{obs} exist at a particular point in the data space. Because the data have measurement uncertainties, the "true" values in the data space may differ from d_{obs}.

Because we have three model parameters across 208 depth points (624 total unknown parameters), our problem spans a high dimensional model space, and an exhaustive search of all possible solutions m is not practical. We limit the number of instances of m to evaluate by using an importance-sampling algorithm. We use a Markov Chain Monte Carlo algorithm to combine *a priori* information about which solutions m are plausible for realistic ice-sheet conditions and information from our data sets. This algorithm efficiently explores the parameter space by favoring instances of m that are similar to those that have already produced good fits with the observations d_{obs}.

In this section, we describe the theoretical framework and the practical implementation of the inverse approach we use. In general, the solution of this type of inverse problem depends on the formulation of the problem, including what information is included in the constraints and how the output is analyzed. We detail below each of the choices that we make in our approach.

S2.1 Bayesian framework

We use a statistical Bayesian framework to solve this inverse problem. Rather than seek a single best-fit solution, we consider the likelihood of different solutions based on probability distributions within the parameter spaces of the data and the model. This framework combines *a priori* model parameter information with data measurement uncertainties. Unlike a regularization approach, such as Tikhonov regularization, a Bayesian approach does not require a subjective choice about how well the final set of solutions should fit the data (Tarantola, 1987; Steen-Larsen et al., 2010).

We characterize the *a priori* information describing the model inputs m as a probability distribution in the model space. This distribution, denoted as $\rho_m(m)$, represents the likelihood of solutions m based on data-independent prior knowledge about what values are realistic for that particular parameter (Mosegaard and Tarantola, 1995; Mosegaard and Sambridge, 2002). To produce the complete solution to the problem, the *a priori* information is combined with the likelihood function, which describes how well the output d from a given solution matches our observations d_{obs}. The likelihood function $L(m)$ is defined as (Mosegaard and Tarantola, 1995):

$$L(m) = C_L \exp(-M(m)), \tag{6}$$

where C_L is a normalization constant and $M(m)$ is a misfit function that measures the deviation between d and d_{obs}.

The likelihood function $L(m)$ is combined with the *a priori* distribution $\rho_m(m)$ to define the *a posteriori* distribution $f(m)$ (Tarantola, 1987):

$$f(m) = C_f L(m) \rho_m(m). \tag{7}$$

The *a posteriori* distribution $f(m)$ contains all the information we have to constrain the inverse problem and thus represents its complete solution. The region of maximum values of $f(m)$ denote the most likely solutions to the problem. This distribution may be Gaussian-like and simple to interpret, or may be multi-modal and require a more complex interpretation. We cannot produce this *a posteriori* distribution analytically, but we can sample its values at discrete points. For each solution m that we test in our forward model G, we calculate a discrete value of $f(m)$.

S2.2 Sampling strategy

Our sampling strategy uses an algorithm to determine which solutions m to test, with the goal of producing $f(m)$ after sufficient iterations (Mosegaard and Tarantola, 1995). The algorithm explores the model space by randomly stepping from one solution m_i to a neighbor m_j. In each iteration, the algorithm follows two stages, designed such that it asymptotically produces $f(m)$ (Mosegaard, 1998; Mosegaard and Sambridge, 2002).

First, an exploration stage defines how the algorithm selects a proposal for m_j given its starting place at m_i. The selection depends on how far in model space the algorithm is allowed to step in a single iteration. While the magnitude and direction of the step are determined randomly, the magnitude is scaled by a base step-size. The choice of base step-size balances the exploration of more of the model space (larger steps) with the exploration of regions that result in high values of $f(m)$ (smaller steps). In practice, we must tune the step size in order to strike this balance (*e.g.* Steen-Larsen et al. (2010)).

Second, an exploitation stage defines the transition probability that the proposed step with be accepted. If the proposed step is rejected, the current solution m_i is repeated for an additional iteration. The simplest choice for the transition probability is the Metropolis acceptance probability (Metropolis et al., 1953; Mosegaard, 1998; Mosegaard and Sambridge, 2002):

$$p_{accept} = min\left(1, \frac{f(m_j)}{f(m_i)}\right). \tag{8}$$

This formulation will always accept the proposed step to m_j if the *a posteriori* distribution is greater at that point ($f(m_j) > f(m_i)$), but may still accept the proposed step even if the *a posteriori* distribution is smaller at that point ($f(m_j) < f(m_i)$) by a probability proportional to $\frac{f(m_j)}{f(m_i)}$. This design prevents the algorithm from getting stuck at a local maximum of $f(m)$, while still favoring samples from regions of the model space with a relatively high value of $f(m)$.

After sufficient iterations, the sampling of this algorithm will converge on $f(m)$. The number of iterations required for convergence, the convergence time, depends on the base step-size chosen. Step size is tuned to minimize the number of iterations required while appropriately sampling the model space. Related to the convergence time is the burn-in time, which refers to the number of iterations completed before the sampled values of $f(m)$ become relatively stationary. After this point, the algorithm continues to sample only highly likely solutions m. Prior work has found that after the burn-in time, the acceptance rate of the algorithm should be 25-50% (Gelman et al., 1996) in order to strike a balance between exploration (bigger steps) and efficiency (smaller steps).

S2.3 Implementation of sampling

To sample and estimate the *a posteriori* distribution, we implement the theory described above. We initiate the problem with our initial guess m_1 for each parameter and begin evaluating successive solutions from that point. Our sampling strategy uses Equation 8 and the associated ideas about sampling efficiency.

In the exploration stage of the algorithm, rather than perturb only one parameter within m_i at a time, all 624 parameters (i.e. values at each depth point for temperature, accumulation rate, and thinning function) are perturbed in each iteration. This design improves the efficiency of the algorithm. Each perturbation is constructed with the same low-frequency, red-noise slope in its power spectral density as that of a comparison data set. The comparison data set for temperature is the water-isotope record, for accumulation rate is a destrained version of the annual-layer thicknesses, and for the thinning function is a DJ-model output. Because in reality we expect temperature, accumulation rate, and thinning to vary smoothly through time, each proposed perturbation must vary smoothly as well. Furthermore, the Δage and diffusion-length data sets are inherently smooth because they integrate information over the depth of the firn column. To prevent spurious high-frequency noise from being introduced into the proposed solution m, we apply a low-pass filter to the perturbation. To the temperature and accumulation-rate perturbations, we apply a lowpass filter at a 3000-year period, which corresponds to the maximum value of Δage. We apply a lowpass filter at a 10,000-year period to the thinning-function perturbations because we expect the thinning function to be even smoother. The perturbations are then added to the previous accepted solution to generate the next proposed solution.

In the exploitation stage, the algorithm determines whether to accept the proposed solution m_{i+1} by calculating and comparing the values of the *a posteriori* distribution at m_i and m_{i+1}. Equation 7 describes how the *a posteriori* distribution is calculated from the likelihood function $L(m)$ and the *a priori* distribution $\rho(m)$. Because we have already incorporated our prior knowledge directly into the model space bounds, we simply compare the value of the likelihood function evaluated at m_i and m_{i+1} (Mosegaard, 1998):

$$p_{accept} = min\left(1, \frac{L(m_{i+1})}{L(m_i)}\right). \tag{9}$$

We define the likelihood function, as in Equation 6, with a misfit function $M(m)$ defined as (Khan et al., 2000; Mosegaard and Sambridge, 2002):

$$M(m) = \sum_n \frac{\left|d^{(n)}(m) - d^{(n)}_{obs}\right|}{\sigma_n}, \tag{10}$$

where $d^{(n)}(m)$ denotes the modeled output, $d^{(n)}_{obs}$ the observation, and σ_n the standard deviation of the observation for the nth datum. This misfit function minimizes the importance of outliers, compared to a root-mean-square formulation.

We run the algorithm until we have 100,000 accepted samples of the *a posteriori* distribution. With an acceptance rate of 30-40%, this requires approximately 300,000 iterations in total. The burn-in time is reached after approximately 10,000 iterations, and we consider solutions m only after this point. We repeat this process five times to account for any persistent impacts from early perturbations, combining all accepted solutions after the burn-in time to create the final set of results. Because only a small perturbation is made between iterations, successive iterations are correlated. Analysis of the *a posteriori* distribution requires a collection of statistically independent models, so we consider only a subset of all accepted models (Mosegaard, 1998; Dahl-Jensen et al., 1998). Through an autocorrelation analysis of the accepted models, we conclude that saving every 300th solution produces a statistically independent set. Out of a total of 500,000 accepted solutions, 1500 solutions are included in our analysis of the *a posteriori* distribution.

Text S3. Sensitivity tests

To determine the extent to which each of our three data sets affects the results, we tested our approach by excluding different combinations of the data sets. We used the same inverse framework as before, but took into account only how well the output d matches the data observations d_{obs} for the data sets included in that test. Excluding all data sets evaluates the effect of the perturbation construction by resampling the *a priori* distribution (Mosegaard and Tarantola, 2002). Figure S2 illustrates that this null test, in which there are *no* constraints from the data, successfully recovers the prior; the mean of the *a priori* distribution is approximately the mean of the bounded model space. This result shows that no spurious information is produced by the sampling procedure.

Building up from the null test, we tested two suites of three runs each to evaluate the sensitivity of results to each of the data sets. The first suite includes only one data set at a time, and the second suite includes two data sets at a time. The results from both suites are similar, and we show here only the results from the second. Figure S3 shows the mean solution from each run of the second suite: excluding Δage (purple), excluding diffusion length (blue), and excluding layer thickness (green), compared alongside the full results including all parameters (black). The right three panels show the effect on the fit of the data parameters, producing, as expected, the worst fit to each data set when that information is excluded from the problem. The left three panels of Figure S3 show how the exclusion of each data set impacts the mean of each set of solutions. The result for the thinning function suggests that, from 40 - 54 ka, the diffusion-length record pulls the thinning function to greater values (less thinning), while the layer thickness pulls the thinning function to smaller values (more thinning). The accumulation-rate reconstruction is most sensitive to diffusion length and layer thickness. The temperature reconstruction is not sensitive to any particular parameter from 0 - 20 ka, but beyond 20 ka, the temperature reconstruction is sensitive to all three datasets.

Text S4. Ice-flow modeling

We use a 2.5-D flowband ice-flow model to estimate a thinning function for SPC14 to compare with the primary thinning function reconstruction described in the main text.

This ice-flow-model thinning function is constrained by data for ages younger than 10 ka, producing an independent data-based estimate of ice thinning. Beyond 10 ka, we do not have sufficient knowledge of past ice flow direction and the associated bed topography along that flow path in order to fully constrain the model. For the older ice, the goal with the ice-flow-model thinning function is to determine if the structure in the primary thinning function is physically plausible. To this end, our flowband modeling suggests that variations in the primary thinning function can indeed be explained by observed variations in bedrock topography.

S4.1 Flowband model

The flowband model was developed to calculate the time-dependent ice-surface evolution and velocity distribution along a flowline in the ice-sheet interior. The model has been described in Koutnik et al. (2016) where it was applied near the WAIS Divide ice-core site. The model calculates the ice-flow field using the Shallow Ice Approximation, which is appropriate for relatively slow-flowing interior ice that is not beneath an ice divide. Necessary boundary conditions and initial inputs to the model include the bed topography, accumulation rate, and ice temperature along the flowline, as well as the ice flux and ice-sheet thickness at one location.

The flow field described by the model is defined within a flowband domain extending 200 km along the flow line. The downstream edge of the domain is located 10 km from the SPC14 site; the upstream edge marks the location of the ice divide, 190 km upstream of the SPC4 site. The width of the flowband domain is a tunable parameter and is determined such that the model matches the measured surface velocities and surface elevations described below (Text S4.2). The ice flux and ice-surface elevation are specified at one point in the domain, which we chose to be near to the drill site.

For this work, we calculate a steady-state flow field, rather than consider the transient response to time-varying forcing. A steady-state model is justified for three main reasons. First, the steady-state model provides a good fit to the observed depth-age relationship for the Holocene (Figure S9), where the flowline location and corresponding bed topography are well defined. Second, temporal variations in the accumulation rate have little impact on the cumulative thinning as a function of depth (e.g. Nye, 1963). We calculate the thinning as a function of depth and then convert to a function of age based on the SP19 timescale (Winski et al., 2019). Third, while accumulation-rate variations and other changes to the boundary conditions affect ice-particle-path trajectories, these inputs require knowledge of the flowline and bed topography, which are poorly known beyond 65 km upstream from SPC14. Without specification of where the ice flowed, we cannot determine these time-variable inputs, and a time-dependent model has limited value. Additionally, we find that a steady-state model satisfies our goal of evaluating the physical plausibility of the primary thinning function reconstruction.

S4.2 Model Inputs

Velocity, elevation, spatial pattern of accumulation rate, and flowline determination: Measurements of the surface velocity, surface elevation, and the determination of the flowline from these measurements are described in Lilien et al. (2018), with data available from the United States Antarctic Program Data Center (USAP-DC) at: https://www.usap-dc.org/view/project/p0000200. The surface velocity was measured at a network of stakes with 12.5 km spacing along the lines of longitude every 10° from 110°E to 180°E and out to a distance of 100 km from SPC14. The modern surface velocities were used to determine the modern flowline. The accumulation-rate pattern along the flowline (Figure S4a) was inferred using traced layers imaged with a 200 MHz radar. By comparing the measured layer thickness in SPC14 to the expected layer thickness due to advection of the upstream accumulation-rate pattern, the flowline was confidently determined for a distance of 65 km upstream of SPC14, spanning the past 10.1 ka (Lilien et al., 2018). For ice older than 10 ka, we are uncertain what path the ice took.

Bedrock topography: The bed topography along the domain of the flowline (from SPC14 to the ice divide) is a necessary model input, and can be grouped into three sections based on the data available. 1) From 0 to 65 km upstream of SPC14, we are confident that the ice flowed over the bedrock topography imaged with radar along the modern flowline. 2) For 65 km to 100 km upstream from SPC14, we use the bedrock topography measured along the modern flowline; however, we cannot be sure that ice reaching the SPC14 site flowed along this path. 3) From 100 km to a divide at approximately 190 km upstream, we have no information about the modern flowline, nor do we know the bed topography. However, we can obtain a plausible example of the bed topography from an airborne radar survey in this region.

For the first and second sections, the bedrock topography along 100 km of the modern flowline upstream of SPC14 was imaged with a ground-based, bistatic impulse radar with center frequency of 7 MHz (Figure S5). The radar system has been used widely in Antarctica (Gades et al., 2000; Neumann et al., 2008; Catania et al., 2010). The radar data and bed picks are posted at the USAP-DC at: https://www.usap-dc.org/view/project/p0000200.

For the third section, to provide additional information about the spatial variability in the bed topography beyond 100 km, we use the PolarGAP airborne radar survey (Forsberg et al., 2017). Although PolarGAP data were collected along 135°E and 142.5°E (Figure S5), the data are publicly available as a gridded product. We interpolate the gridded data to extract the bed topography along the two flight lines. The bed topography along our flowline and the two PolarGAP lines are shown in Figure S6. The three profiles track together well until about 70 km upstream of SPC14 where they diverge as the spacing between the lines increases. To obtain a model input for bed topography that produces thinning variations similar to the primary thinning function (recall that our goal is to evaluate whether these variations are physically plausible), we combine information from the two PolarGAP lines. We connect two points (green circles in Figures S6 and S7) that yield a flowline over a high in the bed topography. The orientation of this flowline is nearly perpendicular to the modern flowline, so the ice is unlikely to have flowed over it; however, this example illustrates that the magnitude of topographic variation required to match the structure of the primary thinning function does exist in the region.

Ice temperature: An ice-temperature profile is specified using a 1-D thermal model fit to the measurements from the AMANDA and IceCube projects (Price et al., 2002), forced to reach the pressure melting point at the bed. This temperature profile is held constant in time and is scaled linearly as a function of ice thickness along the flowline to estimate the full temperature field in our model domain.

Basal melt rate: We test two choices for basal melt rate to gain insight into the sensitivity of the thinning result to this parameter. With all other parameters taken to be the same, one case has no basal melt and one case has 1 cm yr^{-1} of basal melt across the whole domain. A 1 cm yr^{-1} melt rate is similar to the value inferred by Jordan et al. (2018) farther upstream of SPC14. The difference between the resulting thinning functions increases with depth, but varies only by 17% during the last 10,000 years of the core. For simplicity, we plot only the non-basal melt result in Figure 5 of the main text.

S4.3 Tuning the model

We tune the flowband width function and the ice flux out of the downstream edge of the domain in order to approximately match the modern surface velocity, surface elevation, and the approximate divide location (Figure S4). To match the surface velocities where measurements are available, the flowband must narrow from the divide to the core site, consistent with the convergent flow observed in this region. The modeled divide location is 190 km upstream of SPC14 at 3075 m elevation, which matches the likely origin at Titan Dome (Fudge et al., 2020).

S4.4 Comparison with measured layers

The modeled layers are shown in comparison to 7 internal layers imaged by radar (Figure S8). There is a good fit at the core site, which is also reflected in Figure S9, comparing the modeled depth-age profile and the measured data from SP19. The match to the radar layers is not nearly as good upstream where the amplitude of the modeled layers at the bedrock bump is less than what is observed in the measured layers. The discrepancy may be related to the greater uncertainty in the flowband model inputs farther upstream from SPC14.

S4.5 Ice-flow-model thinning function

The ice-flow-model thinning function (Figure 5 in main text) is calculated from the modeled layer thickness at the core site divided by the original thickness (the accumulation rate) when that ice was deposited at the surface. The numerical calculation can become noisy due to the finite model mesh and the difficulty of establishing the accumulation rate at the point of origin given variations in the surface accumulation pattern. Therefore, we smooth the thinning function with a moving average over a depth interval of 50 m. The jaggedness of the thinning function is the most noticeable in the deepest layers where there are smaller depth differences for the same age interval. Because we have used a steady-state model, the modeled age for a given depth is too young for ages prior to the Holocene (since we do not account for the lower accumulation rates of the glacial period). Because the cumulative thinning as a function of depth is insensitive to temporal variations in accumulation (e.g. Nye, 1963), we convert modeled depth to age using the measured depth-age relationship (SP19; Winski et al. (2019)).

The most prominent feature in the thinning function calculated for the Holocene period is at about 7 ka. The $\sim$7 ka layers have thinned less than the layers above, which we term a "reversal" in the thinning function; for example, Parrenin et al. (2004) noted such features for the Vostok ice core. For SPC14, reversals can occur because the strain thinning of layers is affected by changes in ice thickness along the flow line (Figure S10). As the ice flows from a bedrock high into a trough, the thickening of the ice column either reduces the vertical thinning or can even cause vertical thickening. Therefore, ice parcels reaching the $\sim$7 ka layer have thinned less than if the bedrock were flat because the ice column thickened. Ice parcels reaching younger layers, for example the 6 ka layer, have not experienced this thickening. As the ice flows out of this overdeepening, the rise in bed topography causes thinning of the full ice column (e.g. both the 6 ka and 7 ka particles). For the bed topography along the flowline spanning the Holocene time period (from SPC14 to 65 km upstream), this bed overdeepening is the only feature that has a significant impact on the structure of the thinning function.

Text S5. δ^{15}N-based thinning function

We use a thinning function estimated from measurements of δ^{15}N in SPC14 for an additional comparison with the primary thinning function reconstruction described in the main text (Figure 5 in main text). Following Parrenin et al. (2012), the δ^{15}N-based thinning function uses the diffusive column height as calculated from the δ^{15}N measurements and the Δdepth as calculated from the ice age scale to determine how much thinning has occurred since that ice was at the surface (see main text Section 6.1).

We calculate the DCH with (Parrenin et al., 2012):

$$\mathrm{DCH}(t) = \delta^{15}\mathrm{N}(t)\left(\frac{\Delta mg \times 1000}{RT(t)}\right)^{-1}, \tag{11}$$

where Δm is the difference in molar mass between ^{15}N and ^{14}N in kg mol^{-1}, g is the gravitational acceleration (9.81 m s^{-2}), R is the gas constant (8.314 J mol^{-1} K^{-1}), and $T(t)$ is the temperature history in K. We use the temperature reconstruction from the optimization in the main text to estimate the temperature history.

The Δdepth is similar to the Δage except that it is the difference in depth in the core, rather than age, of the same climate event in the ice and gas phases. The Δdepth is found for each gas tie point used to develop the SP19 gas timescale (Epifanio et al., 2020). The depth of the ice of the same age is then found from the SP19 ice timescale (Winski et al., 2019).

The δ^{15}N-based thinning function (Γ) can be described:

$$\Gamma(t) = \frac{\Delta\text{depth}(t)}{\int_0^{\text{LID}(t)} D(z,t)dz} = \frac{\Delta\text{depth}(t)}{\text{LIDIE}(t)} = \frac{\Delta\text{depth}(t)}{A \times \text{LID}(t)}, \qquad (12)$$

where

$$\text{LID}(t) = \text{DCH}(t) + \text{CZ} = \text{DCH}(t) + 3. \qquad (13)$$

$D(z,t)$ is the density profile of the firn relative to density of ice at a given time, LID(t) is the lock-in depth, LIDIE(t) is the lock-in depth in ice equivalent, DCH(t) is the diffusive column height, and CZ is the thickness of the convective zone which we set to 3 m (a typical value found in firn air pumping experiments).

Parrenin et al. (2012) showed that the LID/LIDIE ratio changes relatively little for different climate conditions at Dome C and thus we can use a constant factor to convert LID to LIDIE. We obtain a value of A=0.717 by integrating the SPC14 density profile (Winski et al., 2019) from the surface to a density of 824 kg m^{-3}. In the following sections, we discuss the primary sources of uncertainty in the δ^{15}N-based thinning function.

S5.1 Uncertainties

We estimate the uncertainties in the calculation of this thinning function by calculating the change in the thinning function with a different input for the six main parameters below. We choose values which we believe yield approximately 95% confidence (i.e. 2 standard deviation).

Density and depth of firn column: Converting the LID to LIDIE has two primary uncertainties: how the modern density profile is known and how much variation there is through time. We estimate the first using six firn cores, two at SPC14 and two near South Pole, as well as two at 50 km upstream (Lilien et al., 2018). We assume lock-in density at 824 kg m^{-3} with an uncertainty ± 5 kg m^{-3}. The conversion factor to get LIDIE from LID is equivalent to the average density of the firn column relative to the density of ice, and hence is unitless. To estimate the uncertainty of this conversion factor, we find a maximum difference of 0.015 among the six firn cores relative to measured value for SPC14.

For the time-varying uncertainty, we use the pairs of temperature and accumulation rate for each time step found in the primary reconstruction to force a Herron-Langway densification model. We also allow the surface density to vary by ± 30 kg m^{-3} from the SPC14 surface density value. We find the largest difference from the modern SPC14 value to define an uncertainty of 0.023 (2 standard deviation).

Convective zone impact on diffusive column height: The modern convective zone is 3 m and we assume the uncertainty is ± 3 m.

Vertical thinning of firn column due to ice flow: Separate from firn compaction, there is vertical thinning caused by the lateral stretching due to ice flow. Measurements of englacial vertical velocities have become possible with phase sensitive radars; however, separating the vertical thinning due to ice flow from the vertical compaction of the firn is not yet possible. Therefore, we approximate this vertical thinning assuming a uniform, ice-equivalent vertical strain rate (e.g. Nye, 1963). We develop the uncertainty by assuming either no vertical thinning or double the vertical thinning.

Δdepth: We estimate the uncertainty of the Δdepth from the Δage uncertainties developed for the SP19 gas timescale (Epifanio et al., 2020). To find the uncertainty, we take the difference in depths that correspond to the maximum and minimum gas ages and divide in it in half.

Measurement uncertainty and variability: The DCH is calculated from the δ^{15}N of N_2 data using Equation 11. The uncertainty in determining the DCH depends on three things: 1) the measurement uncertainty of the δ^{15}N; 2) variability in how well the measurement represents the actual DCH; and 3) the uncertainty in interpolation from the closest measurement. The δ^{15}N has been measured at 50- to 100-year resolution for much of the core, such that the interpolation distances are small. To jointly assess these measurement uncertainty and variability, we compared the DCH estimates of the three closest measurements. On average, the three measurements differed by slightly less than 2 m. The differences among the three measurements did not have a temporal trend, so we calculate the uncertainty with a constant 2 m uncertainty. This is the smallest uncertainty for most of the measurements.

S5.2 Total uncertainty on thinning function

To calculate the total uncertainty on the δ^{15}N-based thinning function, we combine the uncertainty calculated for each of the six terms above. The uncertainties for each term are shown in Figure S11. We combine the six sources of uncertainty in quadrature to find the total uncertainty. For glacial-aged ice, the dominant uncertainty is that for Δdepth.

This is driven by the larger uncertainty in Δage primarily due to the larger Δage at WAIS Divide during the glacial. During the Holocene, all of the terms are more similar in magnitude, but the uncertainty due to temporal variations in the density profile is the largest. Our use of a uniform value (.023) for temporal density for the full record is likely too simplistic since the uncertainty is based on glacial values which differ from modern value far more than the Holocene values.

References

Barkan, E and Luz, B. (2007). Diffusivity fractionations of $H_2^{16}O/H_2^{17}O$ and $H_2^{16}O/H_2^{18}O$ in air and their implications for isotope hydrology. *Rapid Communications in Mass Spectrometry*, 21(18), 2999-3005.

Catania, G, C. Hulbe, and H. Conway, 2010. Grounding-line basal melt rates determined using radar-derived internal stratigraphy, *J. Glaciol.* 56(197), 545-554.

Dahl-Jensen, D., Mosegaard, K., Gundestrup, N., Clow, G. D., Johnsen, S. J., Hansen, A. W., and Balling, N. (1998). Past temperatures directly from the Greenland ice sheet. *Science*, 282(5387), 268-271.

Dansgaard, W., and Johnsen, S. J. (1969). A flow model and a time scale for the ice core from Camp Century, Greenland. *Journal of Glaciology*, 8(53), 215–223.

Epifanio, J. A., Brook, E. J., Buizert, C., Edwards, J. S., Sowers, T. A., Kahle, E. C., Severinghaus, J. P., Steig, E. J., Winski, D. A., Osterberg, E. C., Fudge, T. J., Aydin, M., Hood, E., Kalk, M., Kreutz, K. J., Ferris, D. G., and Kennedy, J. A.: The SP19 chronology for the South Pole Ice Core - Part 2: gas chronology, Δage, and smoothing of atmospheric records, Clim. Past Discuss., https://doi.org/10.5194/cp-2020-71, 2020.

Forsberg, R., A.V. Olesen, F. Ferraccioli, T. Jordan, H, Corr and K. Matsuoka (2017). PolarGap 2015/16: Filling the GOCE polar gap in Antarctica and ASIRAS flight around South Pole. Radar grids available at: *ftp : //ftp.bas.ac.uk/tomj/PolarGAP/PolarGAP_radar_grids.zip*

Fudge, T. J., Lilien, D. A., Koutnik, M., Conway, H., Stevens, C. M., Waddington, E. D., Steig, E. J., Schauer, A. J., and Holschuh, N. (2020). Advection and non-climate impacts on the South Pole Ice Core. *Clim. Past*, 16, 819832.

Gades, A.M., C.F. Raymond, H. Conway and R.W. Jacobel, 2000. Bed properties of Siple Dome and adjacent ice streams West Antarctica, inferred from radio-echo sounding measurements. *Journal of Glaciology*, 46(152), 88-94.

Gelman, A., Roberts, G. O., and Gilks, W. R. (1996). Efficient Metropolis jumping rules. *Bayesian Statistics*, 5(599-608), 42.

Gkinis, V., Simonsen, S. B., Buchardt, S. L., White, J. W. C. and Vinther, B. M. (2014). Water isotope diffusion rates from the NorthGRIP ice core for the last 16,000 years - glaciological and paleoclimatic implications. *Earth and Planetary Science Letters*, 405, 132–141.

Johnsen, S. J., Clausen, H. B., Cuffey, K. M., Hoffmann, G., Schwander, J. and Creyts, T. (2000). Diffusion of stable isotopes in polar firn and ice: The isotope effect in firn diffusion. *Physics of Ice Core Records*, 121–140.

Jones, T. R., White, J. W. C., Steig, E. J., Vaughn, B. H., Morris, V., Gkinis, V., Markle, B. R. and Schoenemann, S. W. (2017b). Improved methodologies for continuous flow analysis of stable water isotopes in ice cores. *Atmospheric Measurement Techniques*, 10, 617-632.

Jordan, T. A., Martin, C., Ferraccioli, F., Matsuoka, K., Corr, H., Forsberg, R., Olesen, A., and Siegert, M. (2018). Anomalously high geothermal flux near the South Pole. *Scientific reports*, 8(1), 1-8.

Kahle, E. C. (2020). Climate reconstructions from ice cores: New techniques to understand the information preserved in the South Pole ice core (Doctoral dissertation, University of Washington, Seattle, USA).

Khan, A., Mosegaard, K., and Rasmussen, K. L. (2000). A new seismic velocity model for the Moon from a Monte Carlo inversion of the Apollo lunar seismic data. *Geophysical Research Letters*, 27(11), 1591-1594.

Koutnik, M. R., Fudge, T. J., Conway, H., Waddington, E. D., Neumann, T. A., Cuffey, K. M., Taylor, K. C., et al. (2016). Holocene accumulation and ice flow near the West Antarctic Ice Sheet Divide ice core site. *Journal of Geophysical Research: Earth Surface*, 121(5), 907–924.

Lamb, K. D., Clouser, B. W., Bolot, M., Sarkozy, L., Ebert, V., Saathoff, H., Mohler, O., and Moyer, E. J. (2017). Laboratory measurements of HDO/H2O isotopic fractionation during ice deposition in simulated cirrus clouds. *Proceedings of the National Academy of Sciences*, 114(22), 5612–5617.

Lilien, D. A., Fudge, T. J., Koutnik, M. R., Conway, H., Osterberg, E. C., Ferris, D. G., and Stevens, C. M. et al. (2018). Holocene IceFlow Speedup in the Vicinity of the South Pole. *Geophysical Research Letters*, 45(13), 6557–6565.

Looyenga, H. (1965). Dielectric constants of heterogeneous mixtures. *Physica*, 31(3), 401–406.

Luz, B., and Barkan, E. (2010). Variations of 17O/16O and 18O/16O in meteoric waters. *Geochimica et Cosmochimica Acta*, 74(22), 6276–6286.

Majoube, B. (1970). Fractionation factor of ^{18}O between water vapour and ice. *Nature* 226, 1242.

Metropolis, N., Rosenbluth, A. W., Rosenbluth, M. N., Teller, A. H., and Teller, E. (1953). Equation of state calculations by fast computing machines. *The Journal of Chemical Physics*, 21(6), 1087–1092.

Mosegaard, K., and Tarantola, A. (1995). Monte Carlo sampling of solutions to inverse problems. *Journal of Geophysical Research: Solid Earth*, 100(B7), 12431–12447.

Mosegaard, K. (1998). Resolution analysis of general inverse problems through inverse Monte Carlo sampling. *Inverse Problems*, 14(3), 405.

Mosegaard, K., and Tarantola, A. (2002). Probabilistic approach to inverse problems. *International Geophysics Series*, 81(A), 237–268.

Mosegaard, K., and Sambridge, M. (2002). Monte Carlo analysis of inverse problems. *Inverse problems*, 18(3), R29.

Neumann, T.A., H. Conway, S. Price, E.D. Waddington and D.L. Morse, 2008. Holocene accumulation and ice-sheet dynamics in central West Antarctica. *J. Geophys. Res.*, 113(F2).

Nye, J. 1963. Correction factor for accumulation measured by the thickness of the annual layers in an ice sheet. *Journal of Glaciology*, 4(36), 785788.

Parrenin, F., Barker, S., Blunier, T., Chappellaz, J., Jouzel, J., Landais, A., Veres, D. et al. (2012). On the gas-ice depth difference (Δdepth) along the EPICA Dome C ice core. *Climate of the Past*, 8(2), 1089–1131.

Parrenin, F., F. Remy, C., Ritz, M.J. Siegert, and J. Jouzel, 2004. New modeling of the Vostok ice flow line and implication of the glaciological chronology of the Vostok ice core. *Journal of Geophysical Research*, 109, (D20).

Price, P.B., O.V. Nagornov, R. Bay, D. Chirkin, Y. He,P. Miocinovic, A. Richards, K. Woschnagg, B. Koci and Victor Zagorodnov, 2002. Temperature Profile for Glacial Ice at the South Pole: Implications for Life in a Nearby Subglacial Lake. *Proceedings of the National Academy of Sciences*, 99(12), 7844-7847.

Raymond, C. 1983. Deformation in the vicinity of ice divides. *Journal of Glaciology*, 29(103), 357373.

Schwander, J., Stauffer, B., and Sigg, A. (1988). Air mixing in firn and the age of the air at pore close-off. *Annals of Glaciology*, 10, 141-145.

Steen-Larsen, H. C., Waddington, E. D., and Koutnik, M. R. (2010). Formulating an inverse problem to infer the accumulation-rate pattern from deep internal layering in an ice sheet using a Monte Carlo approach. *Journal of Glaciology*, 56(196), 318-332.

Tarantola, A. (1987). Inverse problem theory: Methods for data fitting and model parameter estimation. *Elsevier*, Amsterdam.

Winski, D. A., Fudge, T. J., Ferris, D. G., Osterberg, E. C., Fegyveresi, J. M., Cole-Dai, J., Buizert, C., Epifanio, J., Brook. E.J., Beaudette. R., Severinghaus. J., Sowers. T., Steig, E.J., Kahle, E.C., Jones, T.R., Morris, V., Aydin, M., Nicewonger, M.R., Casey, K.A., Alley, R.B., Waddington, E.D., Iverson, N.A. (2019). The SP19 chronology for the South Pole Ice CorePart 1: volcanic matching and annual layer counting. *Climate of the Past*, 15(5), 1793–1808.

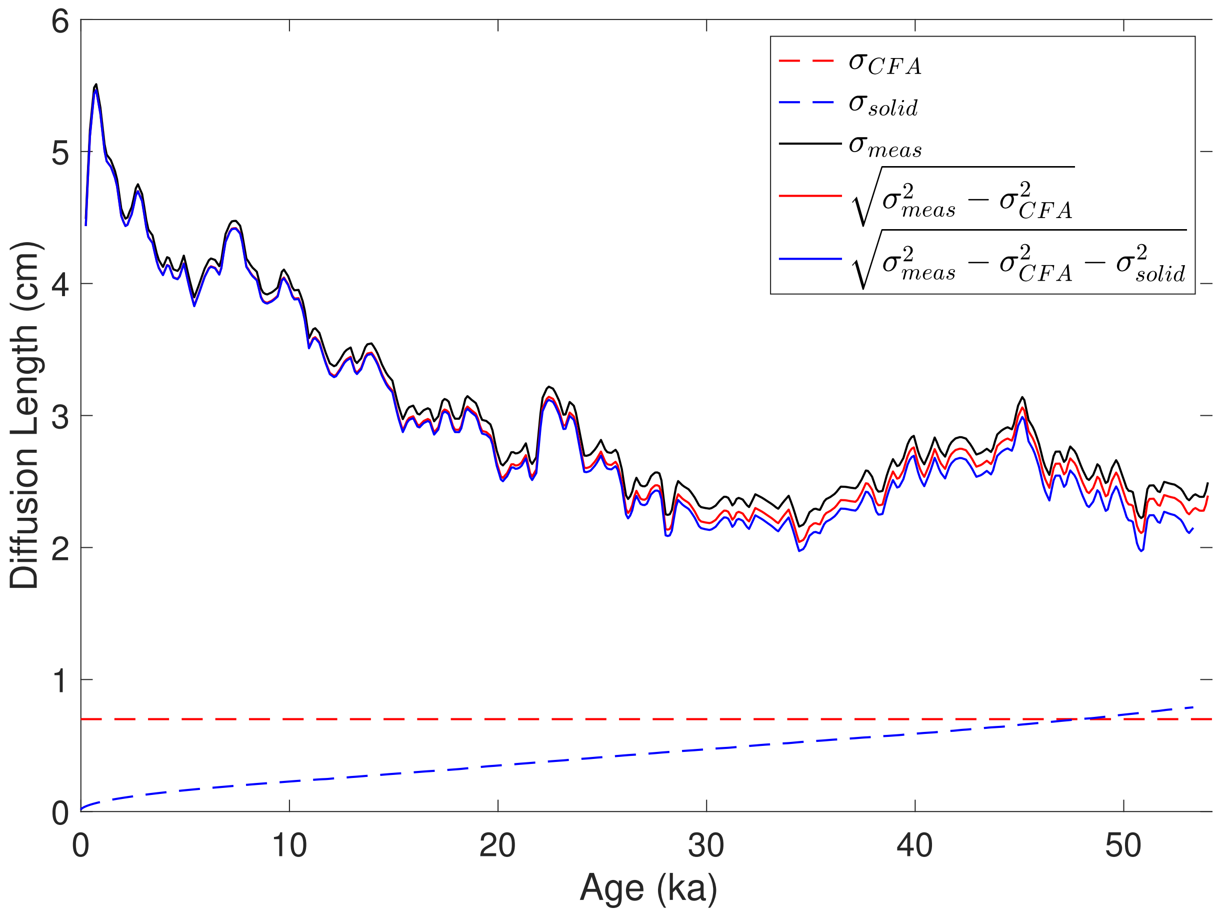

Figure S1: Impact of corrections applied to diffusion-length measurements. Dashed curves show the effective diffusion length resulting from the continuous-flow system (CFA, red), and from diffusion in solid ice (blue). Solid curves show diffusion lengths obtained from the water-isotope data before (black) and after correction for the CFA (red) and solid-ice diffusion (blue).

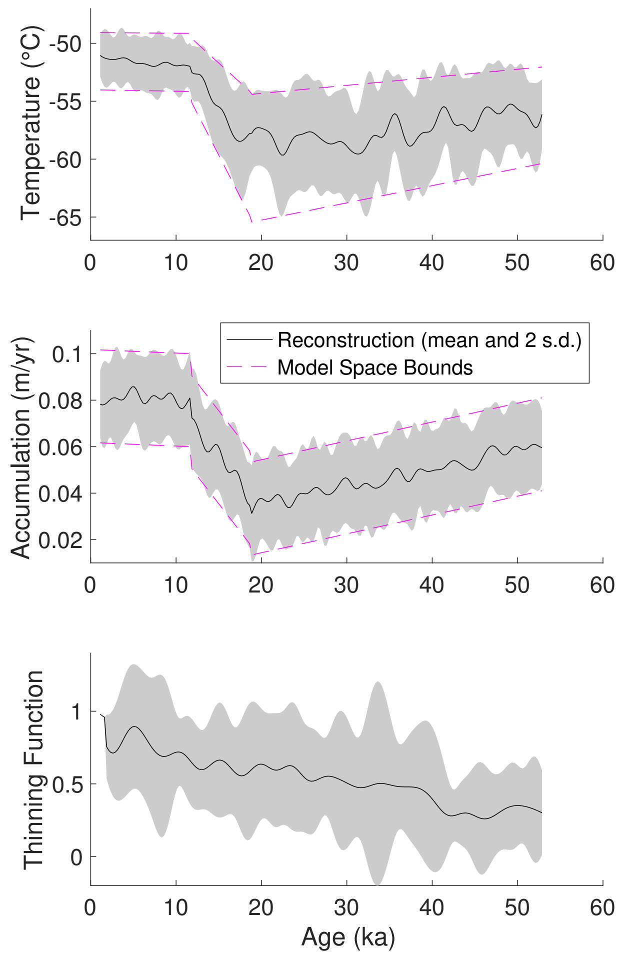

Figure S2: Results of the null-test to recover the *a priori* distribution. In the upper two panels, for which model bounds are defined, two standard deviations of the *a posteriori* distribution (grey shading) approximately fill the bounded space (dashed magenta lines), and the mean of the distribution (black curve) is approximately the mean of the bounds.

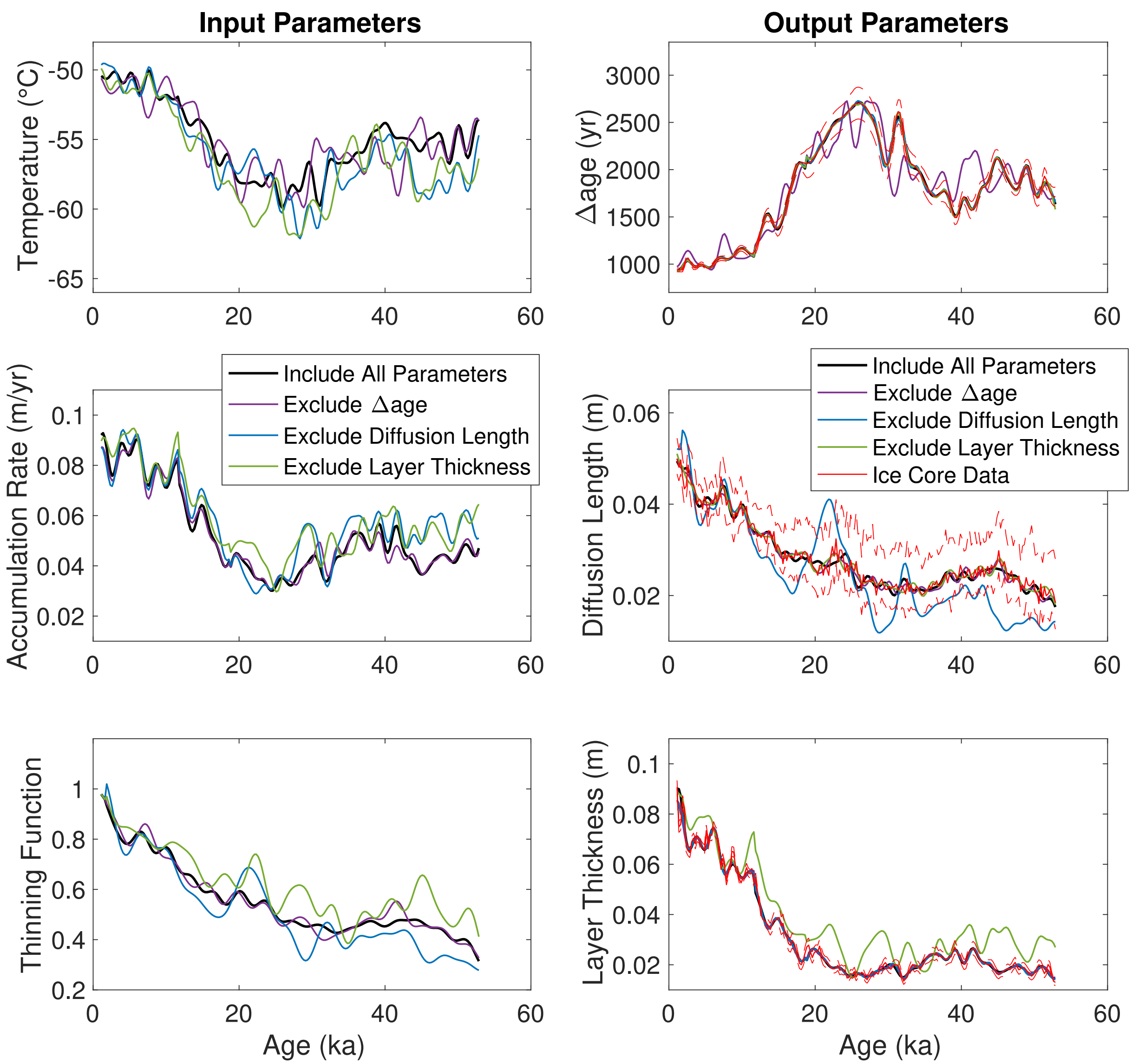

Figure S3: Analysis of the sensitivity of the *a posteriori* distribution to information in each data set. Each color shows the *a posteriori* distribution mean for a different sensitivity test. We compare the results when Δage is excluded (purple), when diffusion length is excluded (blue), when layer thickness is excluded (green), and when all data sets are included (black). Red curves in the right panel show ice-core data and uncertainties.

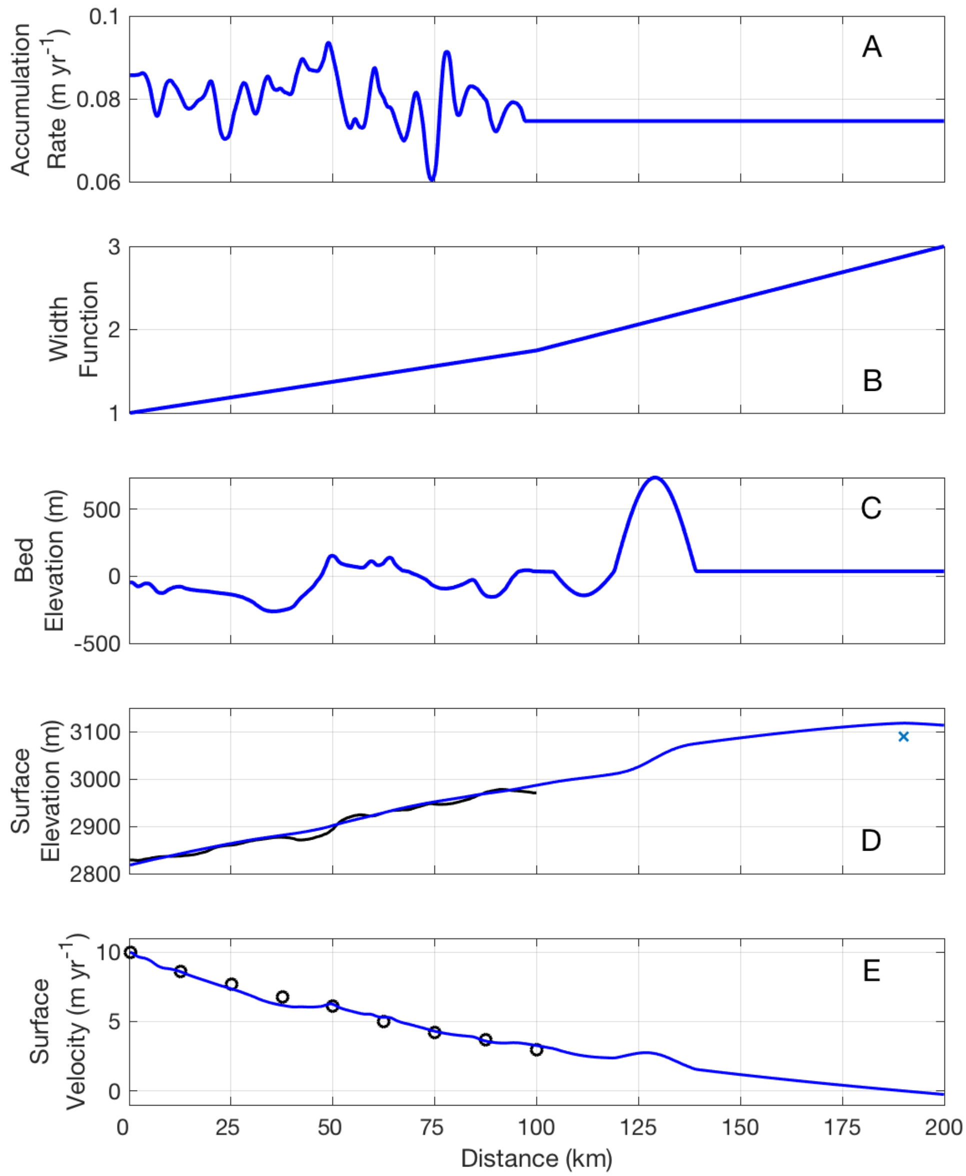

Figure S4: Flowband model inputs (A-C) and model fits to measured data (D-E). A) Modern accumulation-rate pattern for 100 km upstream of SPC14 site inferred from the available shallow radar measurements (Lilien et al., 2018; Fudge et al., 2020). B) Normalized width function used to fit measured surface velocities in panel D. C) Bed topography was measured from 0 to 100 km. Beyond 100 km, the bed topography used in the model is determined as discussed in Text S4.2. D) Measured (black) and modeled surface elevation (blue). The small blue "x" at 190 km marks the approximate position and elevation of Titan Dome relative to SPC14. E) Measured (black circles) and modeled surface velocities (blue).

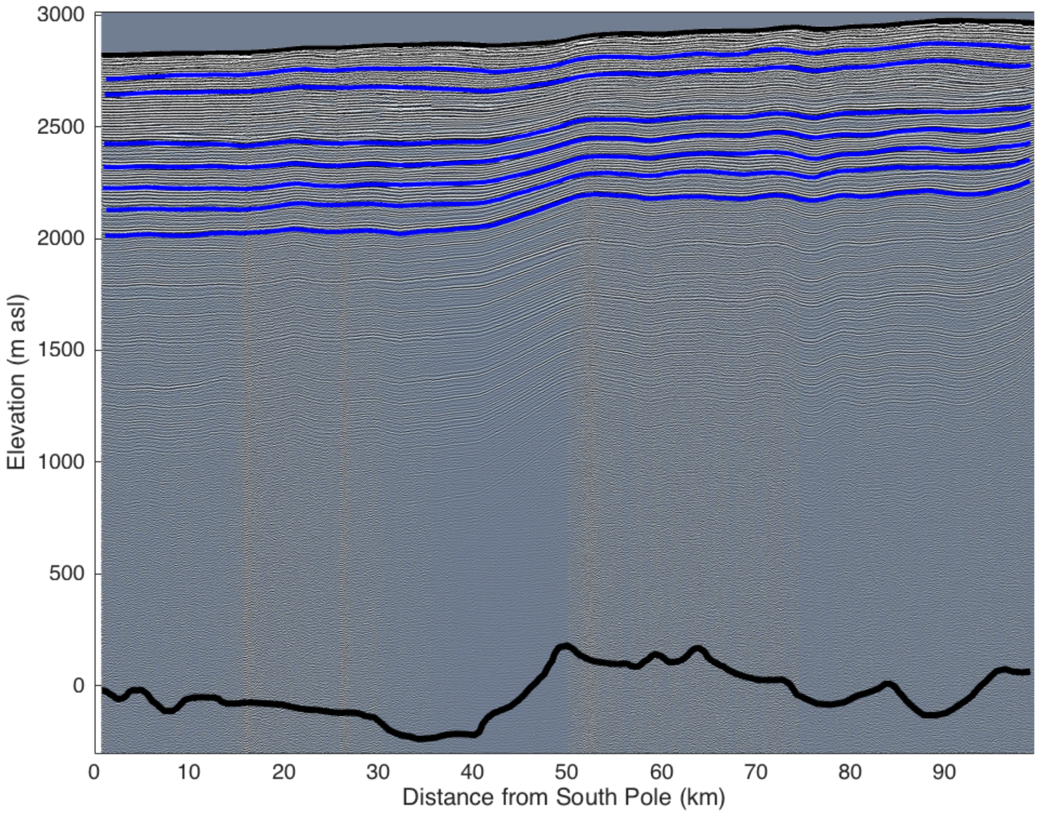

Figure S5: Radar profile along 100 km of the modern flowline upstream of SPC14 (see map, Figure S7). The data were imaged using a ground-based, bistatic impulse radar with center frequency of 7 MHz. The transmitter and receiver were towed inline behind a skidoo; each record consists of 1024 stacked waveforms and records were located using GPS. Reflection positions, measured as a function of radar two-way travel time, were converted to depth below the surface using a wave speed of 168.5 m μs^{-1} in ice and 300 m μs^{-1} in air. Wave speed in the firn was calculated using the density profile from SPC14 and a mixing equation (Looyenga, 1965) to estimate the depth profile of the dielectric constant. Solid black curves show the surface and bed elevations (m above sea level (asl)). Note that the SPC14 site is about 40 m below sea level. Blue curves are radar-detected internal layers (isochrones) that were dated using the SPC14 timescale. Layer ages with increasing depth are: 1020, 1900, 5070, 6510, 8070, 9690, and 11770 years.

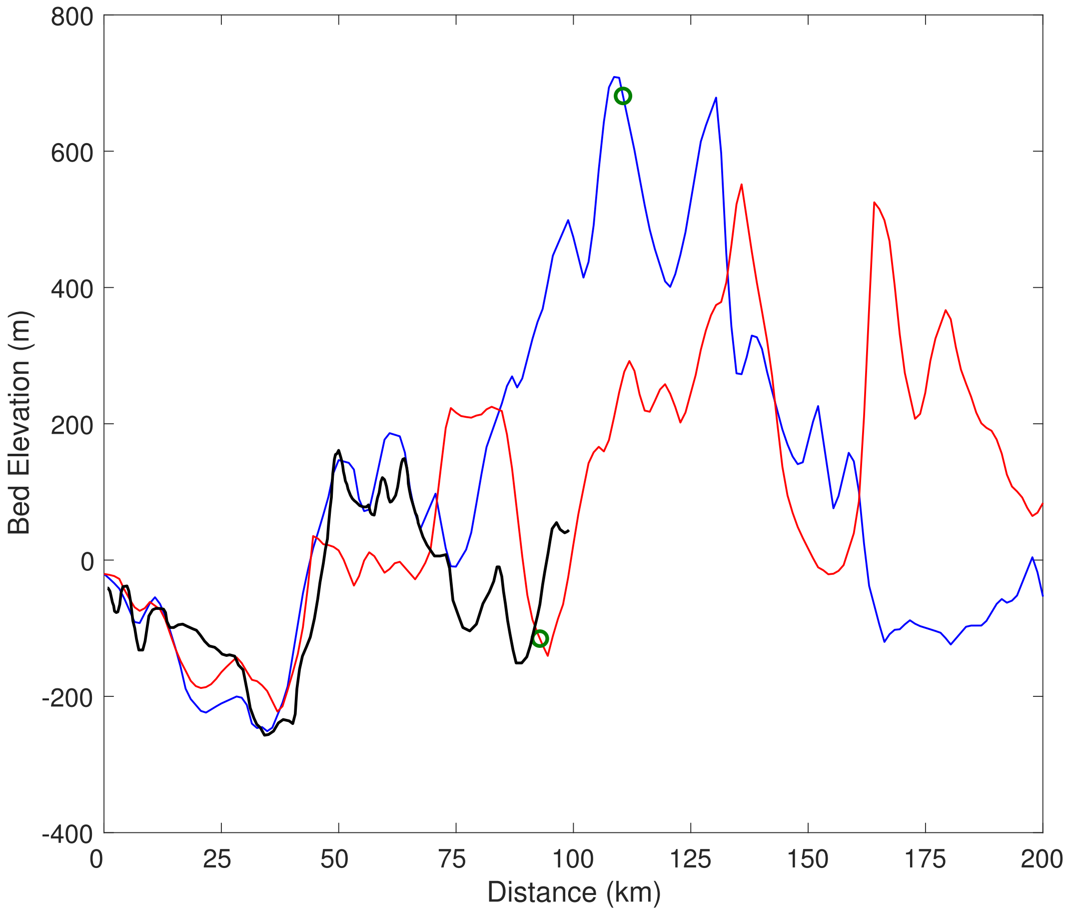

Figure S6: Profiles of bed topography upstream of the SPC14 site. Black is the bedrock measured along the modern flowline. Red is along 142.5°E and blue is along 135°E from the PolarGAP survey. Green circles mark the two points that we use to define a plausible bed feature to explain the thinning function for older ages (circles correspond to Figure S7).

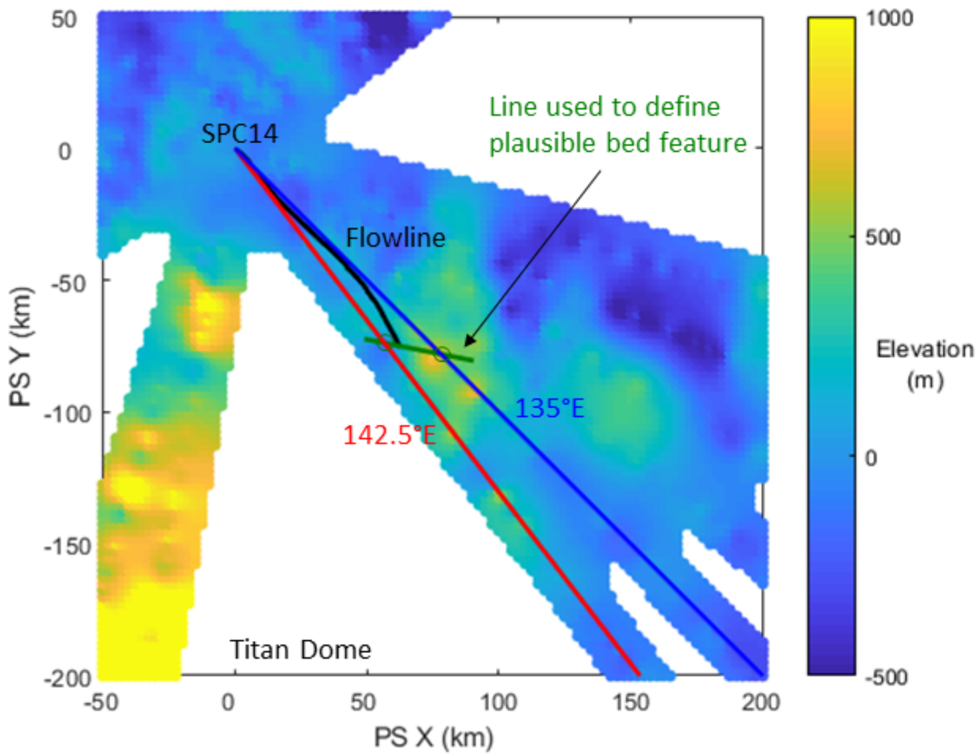

Figure S7: Map view of bed topography near SPC14. Black shows measured flowline. Red is along 142.5°E and blue is along 135°E from the PolarGAP survey. Green line shows the transect between PolarGAP lines used to guide the bed topographic feature beyond 100 km in the ice-flow modeling (circles correspond to Figure S6).

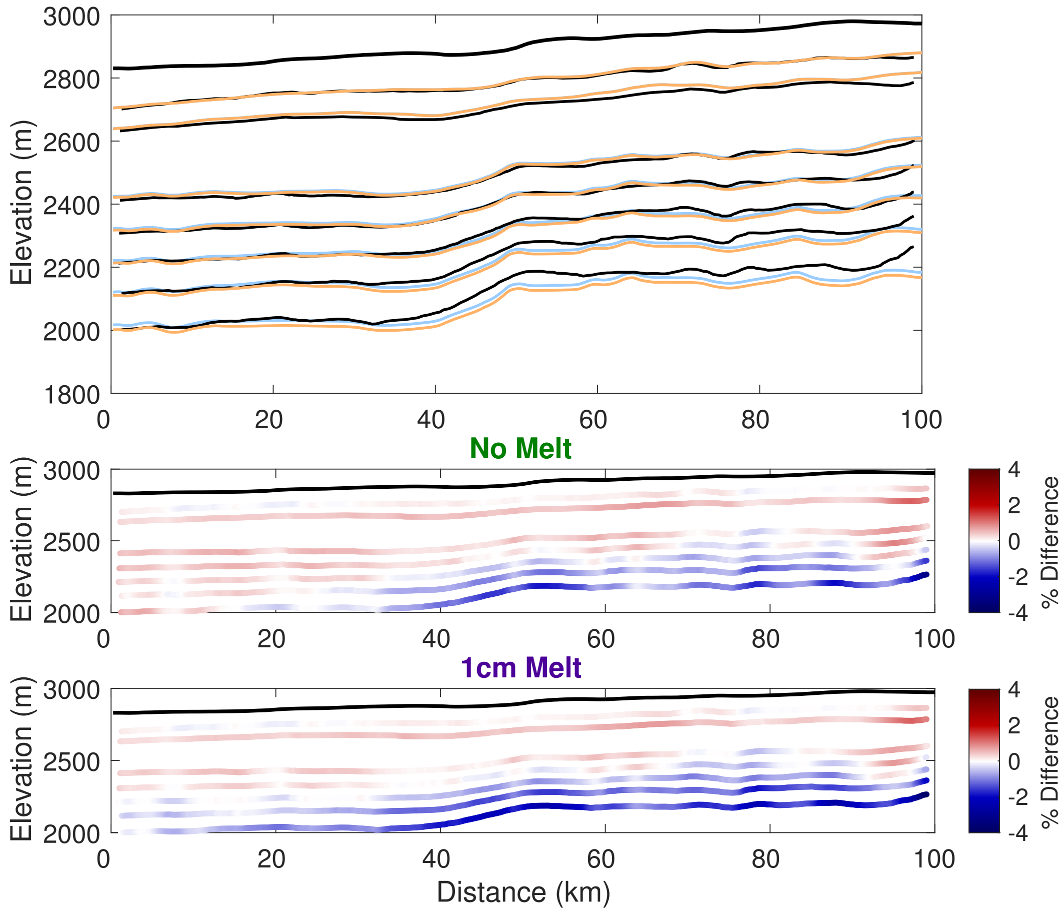

Figure S8: Comparison between modeled and measured internal layers in the flowband domain. Measured layers are shown in Figure S5. A) Observed (black) and modeled with no melt (blue) and 1 cm yr^{-1} melt (orange) internal layers. Observed layer ages are labeled. B) Percent misfit of layer depths for the "no melt" model. C) Percent misfit of layer depths for the "1 cm yr^{-1} melt" model.

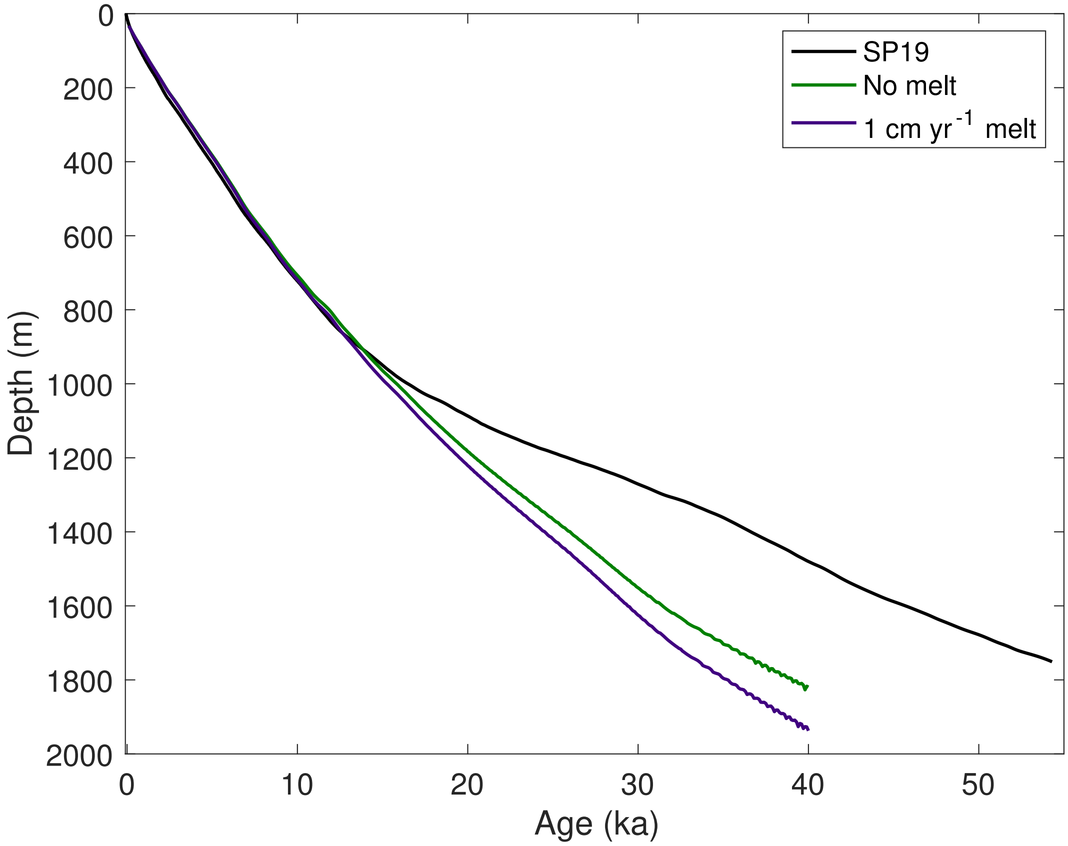

Figure S9: Comparison between modeled and measured depth-age relationship. The depth-age relationship from the steady-state models compare well to SP19 (Winski et al., 2019) for the Holocene. The divergence in the modeled values compared to SP19 values below approximately 900 m depth is due to the decrease in accumulation rate at older ages that we do not simulate with the steady-state model.

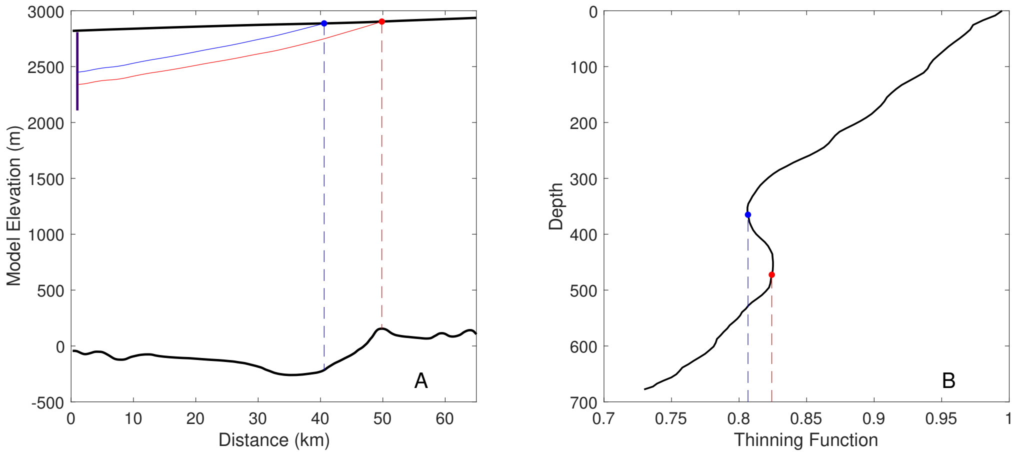

Figure S10: Illustration of the development of a reversal in the thinning function. A) Modeled particle paths with ice thickness (and corresponding bed elevation) at particle origin marked. Age of the red particle is ∼7 ka and age of the blue particle is ∼6 ka. Purple vertical line at the far left side is ice-core location and the depth of the core shows the depth range plotted in B. B) Modeled thinning function showing the reversal in thinning due to thickening of the ice sheet experienced by the red particle but not the blue particle. The jaggedness of the thinning function is due to numerical artifacts in the particle tracking.

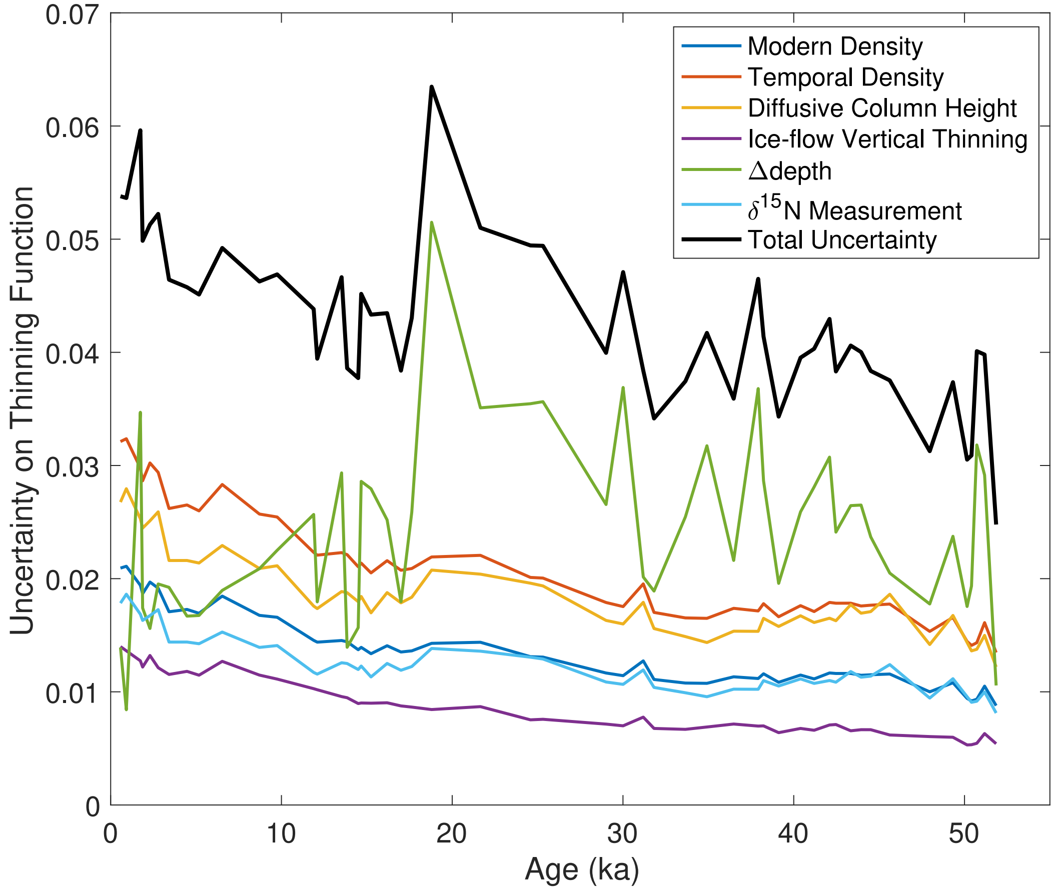

Figure S11: Uncertainty representing two standard deviations for the inferred thinning function from six main sources described in Text S5.1.